SHERLOC Raman Mineral Detections of the Mars 2020 Crater Floor Campaign

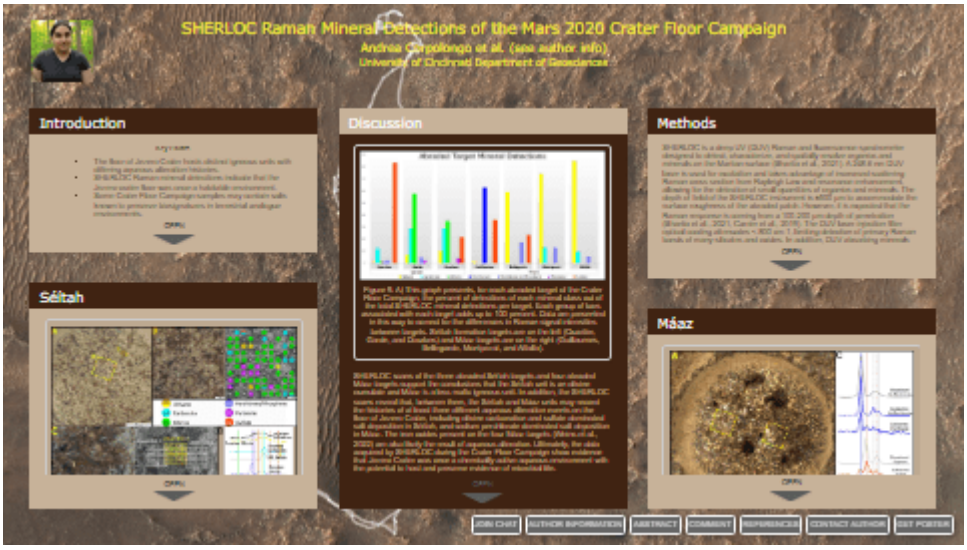

Andrea Corpolongo et al. (see author info)

University of Cincinnati Department of Geosciences

PRESENTED AT:

AGU FALL MEETING
Chicago, IL & Online Everywhere
12–16 December 2022

SCIENCE LEADS THE FUTURE

ABSTRACT

During the first science campaign of the Mars 2020 mission, Perseverance rover's Scanning Habitiable Environments with Raman and Luminescence for Organics and Chemicals (SHERLOC) deep UV Raman and fluorescence instrument collected microscale, two-dimensional Raman and fluorescence images on ten natural and abraded targets on two different Jezero crater floor units: Séítah and Máaz. SHERLOC Raman images collected during the Crater Floor Campaign indicate that Séítah and Máaz are mineralogically distinct igneous units with complex aqueous alteration histories. SHERLOC data show that Séítah is olivine-rich with evidence of olivine carbonation, while Máaz features widespread silicates, but lacks olivine. Both units feature salt deposits. In Séítah, the salts are predominantly sulfate. Where salts are observed in Máaz, they are a mixture of sodium perchlorate and sulfates. Taken together, SHERLOC data collected during the Crater Floor Campaign suggest that the Jezero crater floor once hosted an environment capable of supporting microbial life and preserving evidence of that life, if it existed.

INTRODUCTION

Key Points

- The floor of Jezero Crater hosts distinct igneous units with differing aqueous alteration histories.
- SHERLOC Raman mineral detections indicate that the Jezero crater floor was once a habitable environment.
- Some Crater Floor Campaign samples may contain salts known to preserve biosignatures in terrestrial analogue environments.

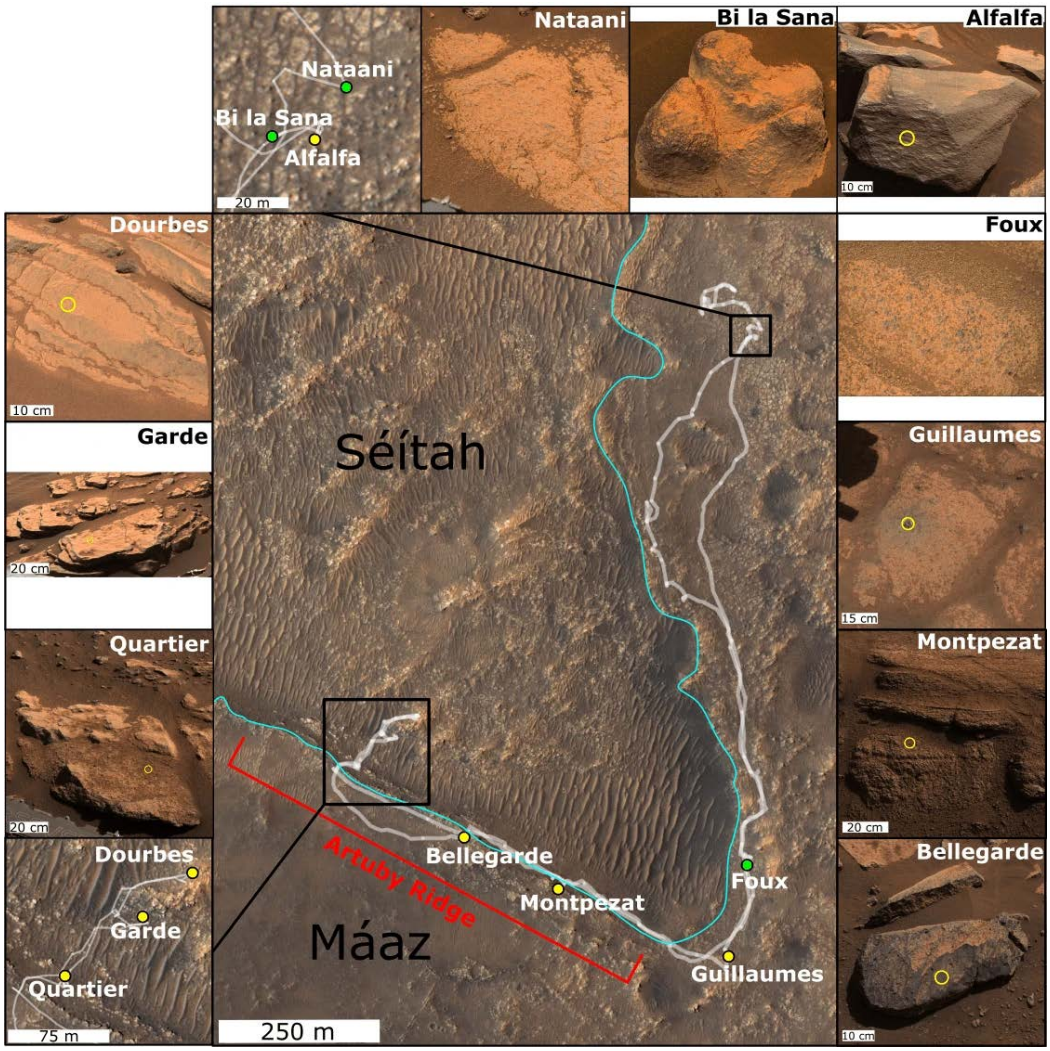

Figure 1. Map of the Crater Floor Campaign traverse (central image and insets, based on HiRISE imagery) and natural and abraded targets analyzed by proximity science, including SHERLOC and WATSON, through sol 370 (smaller images around the periphery, imaged by the MastCam-Z instrument on the Perseverance rover). The white path on the map shows Perseverance's traverse. The cyan line marks the approximate contact between the Séítah formation below and the Máaz formation above. The red bracket indicates Artuby Ridge. Targets analyzed are indicated along the route. The yellow circles on most targets indicate the location of abrasion patches (see subsequent figures). Those without yellow circles were not abraded. The scans on unabraded patches yielded no discinerable Raman signal.

The Crater Floor Campaign was an exploration of the floor of Jezero crater (Sun et al., 2022; Fig. 1). During this campaign, the rover investigated two major units, Séítah and Máaz, which had been identified from orbital data before surface operations commenced (Stack et al., 2020). The older unit, Séítah, previously referred to as the Crater Floor Fractured 1 (CF-F-1) Unit, is light-toned, ridged, and fractured. Séítah is overlain by Máaz, previously referred to as the Crater Floor Fractured Rough (CF-Fr) Unit, which is light-toned and polygonally fractured. Results from the Perseverance payload during the Crater Floor Campaign indicate that both Máaz and Séítah are igneous in origin (Horgan et al., 2022). Máaz is characterized by the presence of abundant pyroxene (Schmidt et al., 2022; Udry et al., 2022), while Séítah is an olivine cumulate (Brown et al., 2022; Farley et al., 2022; Liu et al., 2022; Nuñez et al., 2022; Wiens et al., 2022). The transition between the Séítah and Máaz units is highlighted in cyan in Figure 1.

The Crater Floor Campaign addressed several objectives of the Mars 2020 mission by contributing to a scientific understanding of the geology of Jezero crater, seeking rocks with a high probability of preserving ancient biosignatures and looking for potential biosignatures within rocks of the Séítah and Máaz units, and documenting the geological context of the first set of samples collected for possible future return to Earth. This poster presents spectral maps collected by SHERLOC (Scanning Habitable Environments with Raman and Luminescence for Organics and Chemicals), an arm mounted deep UV (DUV) Raman spectrometer (Bhartia et al., 2021). The maps are paired with high resolution (10.1 μm/pixel) grayscale images collected by the co-boresighted Autofocus Contex Imager (ACI), enabling mapping of the location where each Raman spectrum was collected on the target surface. In addition, the Wide Angle Topographic Sensor for Operations and eNgineering camera (WATSON) provides macro-scale, color images of the Raman scan targets. Combining the image color of WATSON images with the high resolution of the ACI images produces colorized ACI images that can allow for the identification of individual mineral grains.

SÉÍTAH

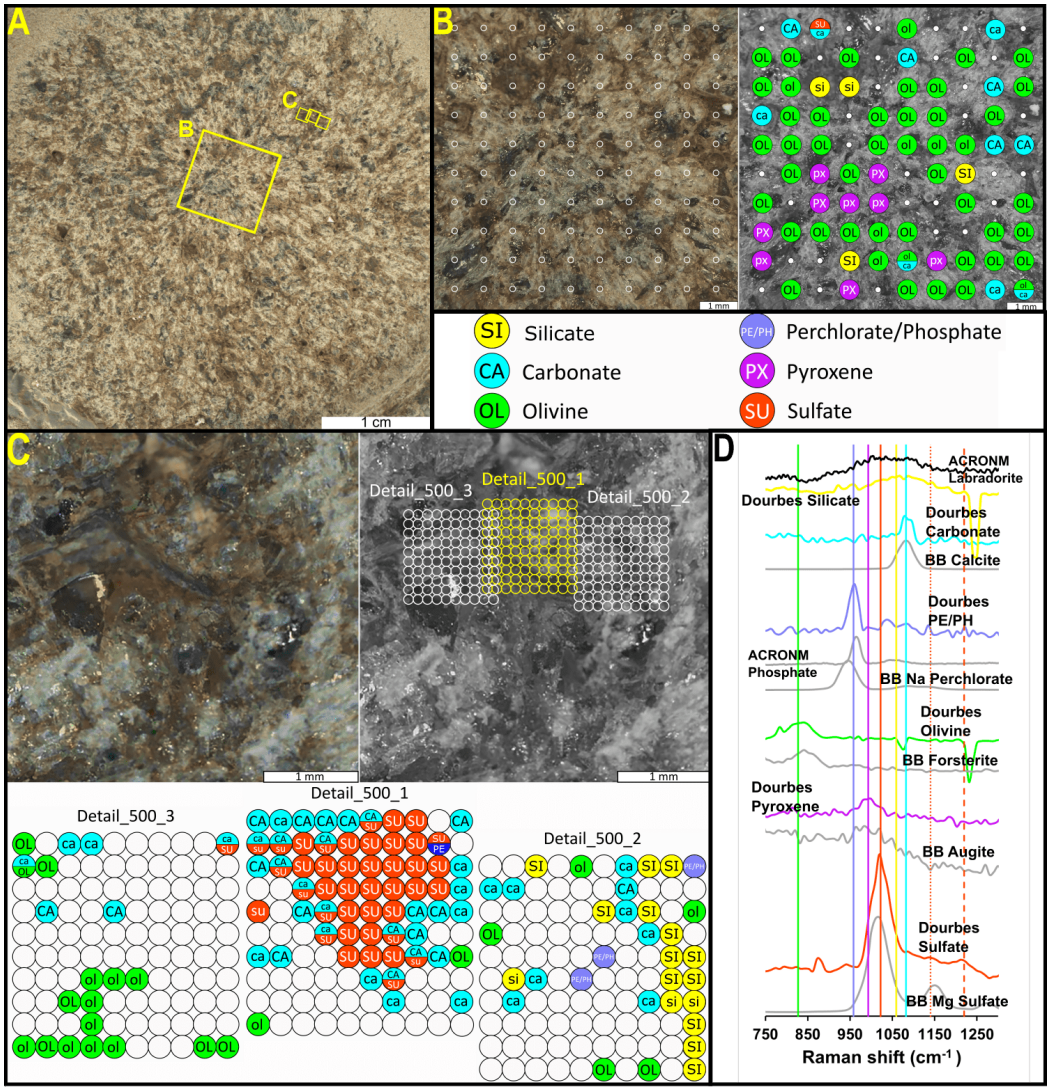

Figure 2. SHERLOC Raman mineral identifications from Dourbes.

A) The abrasion patch imaged by WATSON (image ID SI1_0257_0689775622_738FDR_N0080000SRLC00006_000095J01). Yellow boxes indicate the location of the scans performed. B) Colorized (left) and grayscale (right) ACI images (image ID SC3_0257_0689786306_125FDR_N0080000SRLC11421_0000LMJ01) of the region of the abrasion patch bounded by the larger yellow box in panel A. The white circles in panel B indicate the locations of SHERLOC analysis spots. Mineral identifications are indicated in the right panel. C) Colorized (left) and grayscale (right) ACI images (image ID SC3_0269_0690851147_347FDR_N0080000SRLC11373_0000LMJ02) of the region of the abrasion patch bounded by the smaller yellow boxes in panel A. The white and yellow circles in the upper right subpanel of panel C indicate the locations of SHERLOC analysis spots for three 1 mm^2 Detail scans. The lower three subpanels show mineral identifications for these three Detail scans. D) Representative Raman spectra of minerals detected with high confidence from the abrasion patch and spectra of mineral standards collected on the SHERLOC Brassboard instrument at JPL and the ACRONM instrument at JSC. Vertical lines indicate peak centers. Spectra are offset along the y-axis for clarity.

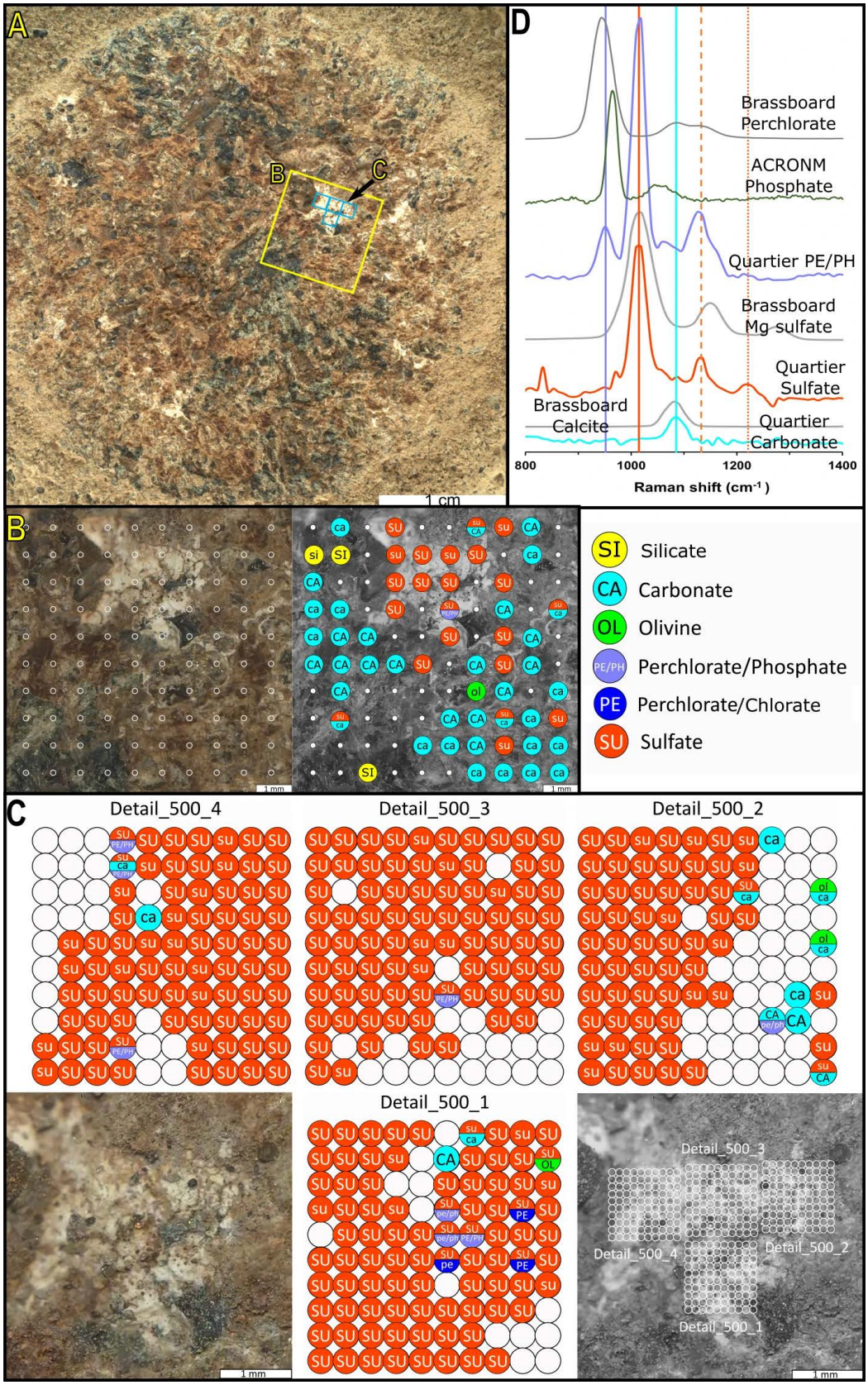

Figure 4. SHERLOC Raman mineral identifications from Quartier. A) The abrasion patch imaged by WATSON (image ID SIF_0292_0692866773_550FDR_N0090000SRLC00702_0000LMJ01). The yellow box indicates the location of the HDR scan and blue boxes indicate the location of the Detail scans. B) Colorized (left) and grayscale (right) ACI images (image ID SC3_0293_0692982585_671FDR_N0090000SRLC10600_0000LMJ01) of the region of the abrasion patch bounded by the larger yellow box in panel A. The white circles in panel B indicate the locations of SHERLOC analysis spots for 0293_Quartier HDR_500_1. Mineral identifications are indicated in the

right panel. C) Colorized (bottom left) and grayscale (bottom right) ACI (image ID SC3_0304_0693962423_667FDR_N0090000SRLC11373_0000LMJ01) images of the region of the

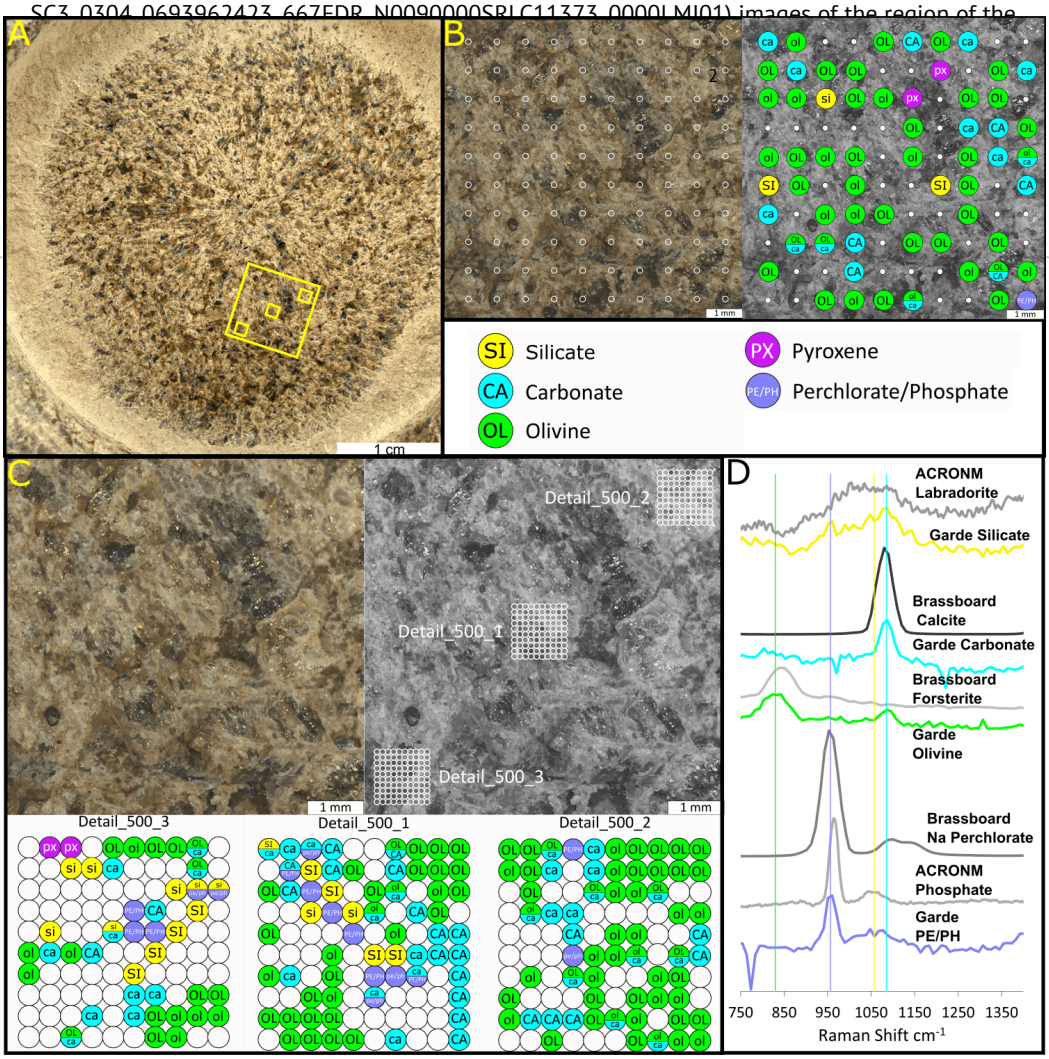

Figure 3. SHERLOC Raman mineral identifications from Garde. A) The abrasion patch imaged by WATSON (image ID SIF_0206_0685226491_804FDR_N0071836SRLC01024_0000LMJ01). Yellow boxes indicate the location of scans. B) Colorized (left) and grayscale (right) ACI images (image ID SC3_0208_0685436606_980FDR_N0071836SRLC11372_0000LMJ01) of the region of the abrasion patch bounded by the larger yellow box in panel A. The white circles in panel B indicate the locations of SHERLOC analysis spots for scan 0207_Garde HDR_500_2. Mineral identifications are indicated in the right panel. C) Upper Panel: Colorized (left) and grayscale (right) ACI images (image ID SC3_0208_0685432316_968FDR_N0071836SRLC11370_0000LMJ01) of the region of the abrasion patch where the Detail scans occurred. The white circles on the grayscale ACI image in panel C indicate the locations of SHERLOC analysis spots of three 1 mm^2 Detail scans. The lower subpanel shows mineral identifications for the Detail scans. D) Representative Raman spectra of minerals detected with high confidence and spectra of mineral standards collected on the SHERLOC Brassboard instrument at JPL. Vertical lines indicate peak centers. Spectra are offset along the y-axis for clarity.

DISCUSSION

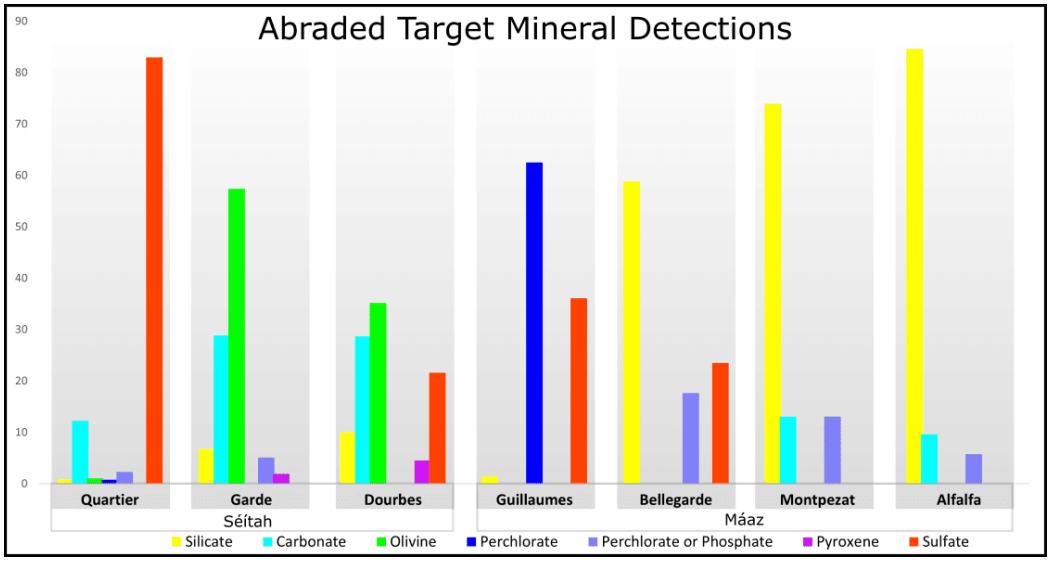

Figure 9. A) This graph presents, for each abraded target of the Crater Floor Campaign, the percent of detections of each mineral class out of the total SHERLOC mineral detections per target. Each group of bars associated with each target adds up to 100 percent. Data are presented in this way to correct for the differences in Raman signal intensities between targets. Séítah formation targets are on the left (Quartier, Garde, and Dourbes) and Máaz targets are on the right (Guillaumes, Bellegarde, Montpezat, and Alfalfa).

SHERLOC scans of the three abraded Séítah targets and four abraded Máaz targets support the conclusions that the Séítah unit is an olivine cumulate and Máaz is a less mafic igneous unit. In addition, the SHERLOC scans reveal that, between them, the Séítah and Máaz units may record the histories of at least three different aqueous alteration events on the floor of Jezero Crater, including olivine carbonation and sulfate dominated salt deposition in Séítah, and sodium perchlorate dominated salt deposition in Máaz. The iron oxides present on the four Máaz targets (Weins et al., 2022) are also likely the result of aqueous alteration. Ultimately, the data acquired by SHERLOC during the Crater Floor Campaign show evidence that Jezero Crater was once a chemically active aqueous environment with the potential to host and preserve evidence of microbial life.

Figure 9 shows that the three most common mineral class detections in SHERLOC scans of Séítah targets were olivine, carbonate, and sulfate. Olivine and carbonate detections dominated scans in targets Dourbes and Garde, while minimal olivine was detected in Quartier. Scans of Quartier and Dourbes both revealed patches of sulfate, while Garde scans detected no sulfate. The minimal olivine detections in Quartier and lack of sulfate detection in Garde may not reflect a major difference in the mineralogy of these targets. The discrepancies may, instead, reflect the SHERLOC team's decision to focus Quartier scans on the bright white patches of the target and the patchy nature of salt deposits in the Séítah formation.

We observe gray grains similar to the one that corresponds with a definitive olivine spectrum in 0304_Quartier Detail_500_1 across the surface of Quartier, sometimes rimmed by light reddish-brown material (Fig. 4A). These gray grains appear similar to grains identified as olivine in Dourbes and Garde and the reddish-brown material looks similar to carbonate that was associated with the olivine in Dourbes and Garde (Figs. 2, 3). While it is possible that Bastide, the outcrop that hosted the Garde abrasion (Fig.1), contains no sulfate deposits, it is equally likely that the Garde abrasion and scans simply did not sample Bastide's sulfate deposits. As demonstrated by the sulfate detected in Dourbes (Fig. 2), Séítah sulfate deposits are not all as visually prominent as the sulfate detected in Quartier (Figs. 4).

The closely associated olivine and carbonate detections in Garde and Dourbes suggest that the olivine cumulate Séítah unit was exposed to at least one aqueous alteration event, during which partial carbonation of olivine took place (Figs. 2 and 3). In particular, detail maps of Dourbes reveal a euhedral olivine crystal with no directly associated carbonate sitting less than one millimeter away from a subhedral olivine grain with adjacent carbonate grains (Fig. 2C). Sulfate deposits in

both Dourbes and Quartier are rimmed by carbonate that is both spectrally and morphologically similar to the carbonate associated with olivine in Dourbes and Garde (Figs. 2, 3, 4). This suggests that all of the carbonates in Séítah formed via the same process, olivine carbonation, and that Séítah's sulfate was deposited later by a sulfate-rich brine, in pore space generated during olivine carbonation through cracking caused by the pressure of carbonate crystal formation (e.g., Xing et al., 2018).

Farley et al. (2022) report that the totality of data collected during the Mars 2020 Crater Floor campaign indicates that the Máaz and Séítah units either originated from two different sources or represent different layers of a single differentiated magma body. The different rock-forming mineral detections of (non- olivine or pyroxene) silicate in the Máaz targets Bellegarde, Montpezat, and Alfalfa, and olivine and pyroxene detections in Séítah targets further supports Farley et al.'s interpretation (Fig. 9). SHERLOC's microscale mapping of Máaz targets reveals that similar spectra assigned to silicate correspond to grains with very different morphologies. Silicate detections in Montpezat and Bellegarde map to sub-millimeter dark blue-gray grains; in Alfalfa, the detections correspond to mm-scale reflective white lathe-like crystals (Figs. 6-8). Although the (non- olivine or pyroxene) silicate spectra reported above were all compared to the same standard labradorite spectrum, the broad bands that led us to assign the spectra to silicate are centered at different wavenumbers: 1050 cm-1, 1036 cm-1, and 1053 cm-1 in Montpezat, Bellegarde, and Alfalfa, respectively. The variable grain morphology and Raman band placement in Máaz silicate detections suggests that they correspond to at least two different silicate mineral species.

Perchlorate and sulfate detected in Guillaumes and Bellegarde scans are evidence of a third possible aqueous alteration event on the floor of Jezero Crater. While the Guillaumes and Bellegarde salt deposits are similar in morphology to the deposits in Dourbes and Quartier, they differ in mineralogy. The deposits in Dourbes and Quartier were predominantly sulfate, with only minor perchlorate contributions. In contrast, SHERLOC mineral detections on the white patch of minerals in Guillaumes were dominated by perchlorate that can, in some cases, be identified as sodium perchlorate, with lesser, but still significant, sulfate contributions. SHERLOC scans of Bellegarde detected sulfate signatures alongside perchlorate or phosphate signatures and SuperCam detected a sodium perchlorate signature (Meslin et al., 2022). Taken together, these SHERLOC and PIXL detections suggest that the salts in Guillaumes and Bellegarde precipitated from a perchlorate-sulfate-bearing brine as it percolated through the Máaz formation rocks.

The mineral detections discussed above are consistent with a changing, habitable aqueous environment that was capable of supporting microbial life and preserving evidence of that life, if it existed. In low-temperature terrestrial environments, carbonation of mafic to ultramafic rocks, which SHERLOC data from Séítah formation targets indicate occurred in the Jezero Crater lake, produces hydrogen that can fuel low-density microbial communities (e.g. Fones et al., 2019; Twing et al., 2017; Woycheese et al., 2015). Terrestrial sulfate and perchlorate brines, similar to the brines that likely deposited the sulfate and perchlorate that SHERLOC detected in Jezero Crater, can host microbial life (e.g., Cesur et al., 2022: Fox-Powell & Cockell., 2018; Heinz et al., 2019, 2020). Furthermore, terrestrial sulfate minerals can trap and preserve organic molecules within their structure (eg., Aubrey et al, 2006; Kotler et al., 2008; Schopf et al., 2012; Shkolyar and Farmer, 2018), and halite- and perchlorate-rich hypersaline subsurface deposits in the Atacama Desert can preserve organic molecules for millions of years (Fernández-Remolar et al., 2013).

METHODS

SHERLOC is a deep UV (DUV) Raman and fluorescence spectrometer designed to detect, characterize, and spatially resolve organics and minerals on the Martian surface (Bhartia et al., 2021). A 248.6 nm DUV laser is used for excitation and takes advantage of increased scattering Raman cross section from Rayleigh Law and resonance enhancement, allowing for the detection of small quantities of organics and minerals. The depth of field of the SHERLOC instrument is ±500 µm to accommodate the surface roughness of the abraded patch. However, it is expected that the Raman response is coming from a 100-200 µm depth of penetration (Bhartia et al., 2021, Carrier et al., 2019). The DUV laser-injection filter optical coating attenuates < 800 cm-1, limiting detection of primary Raman bands of many silicates and oxides. In addition, DUV absorbing minerals (i.e., some Fe containing minerals) can attenuate the depth of penetration into a material and reduce signal to noise ratios (SNR) (Morris et al., 2022; Razzell Hollis et al., 2021a).

SHERLOC is an arm-mounted instrument, which allows it to be moved into proximity of an analysis target. With no change in arm position, an internal scanning mirror rasters the DUV laser beam across the sample surface. With a maximum area of 7 x 7 mm, Raman/fluorescence spectra are acquired at discrete points with a beam diameter of ~100 µm (Bhartia et al., 2021). Prior to each spectrum scan, the Autofocus Context Imager (ACI) is used to acquire 10.1 µm/pixel resolution grayscale images of the target surface. This provides context for the spectral maps and is used to focus the spectrometer/laser. Color images acquired by WATSON have a spatial resolution ranging from 16 to 150 µm/pixel and are used for targeting SHERLOC observations and textural analysis (Bhartia et al., 2021; Edgett et al., 2012). SHERLOC is designed to simultaneously collect Raman and fluorescence data on the same CCD with a single readout. To reduce noise, the CCD readout is binned into 3 regions, a Raman region ~ 800 to 4000 cm−1 (250 to 273 nm) and two fluorescence regions (274 to 337 and 338 to ~370 nm). Each region has a separate wavenumber calibration, previously discussed in detail (Uckert et al., 2021).

Scan Procedures

We use the following nomenclature to describe SHERLOC Raman measurements (Fig. S1). A “target” refers to the specific rock or abraded patch on which data were collected, such as “Nataani” or “Guillaumes,” while a “scan” refers to a specific Raman hyperspectral map that was collected on a target. Each Raman scan is named using the nomenclature “#0001_name_#2_#3”, wherein #0001 denotes the sol on which the scan was performed, name refers to the target and describes the parameters of the scan, #2 is the laser pulses per each point spectrum within a scan, and #3 is the scan number used to differentiate between multiple scans of the same parameter made on the same sol. Each individual spectrum within a scan is referred to as a “point,” and each point within a scan is assigned a number according to the order it occurred in the scan. The first Raman spectra collected within a scan falls at the upper left corner of the hyperspectral map. Collection continues in a serpentine pattern, such that the final spectra in a 100 point scan falls at the lower left corner of the map. High Dynamic Range (HDR) scans consist of 100 points with 780 µm spacing for an image size of 7 x 7 mm. Detail scans consist of 100 points with 100 µm spacing for an image size of 1 x 1 mm. Survey scans consist of 1296 points with fixed spacing between them (50, 144, or 200 µm, depending on the scan template) and 10 or 15 pulses per point. For example, the scan name “0083_Nataani HDR_50_1” describes the first HDR scan performed on Nataani using 50 pulses per point on sol 83 of the Mars 2020 mission.

For each scan SHERLOC performs, single spectra are obtained by first collecting a dark spectrum with no incident laser light and then collecting the active spectrum with the laser firing. The dark scan is then subtracted from the active spectrum to produce the reported Raman spectrum. SHERLOC spectra have a ~10 cm-1/pixel resolution with a Raman spectral range of ~800–4000 cm-1. The potential to observe Raman bands in the spectral range below 800 cm-1 is limited because SHERLOC’s laser-injection filter has reduced transmission in this region and the 252.9 nm laser plasma line is observed at ~650 cm-1. However, very strong bands below 800 cm-1 can be observed (Bhartia et al., 2021; Uckert et al., 2021; Razzell Hollis et al., 2021a).

We performed scans on both natural and abraded targets. Targets were abraded using Perseverance’s Rock Abrasion Tool (RAT), which is ~45 mm in diameter and capable of creating smooth-bottomed abraded patches up to ~1 cm deep. After abrasion, abraded patches are cleaned of dust and cuttings by the gaseous dust removal tool (gDRT), which blasts the abraded target with a high-velocity jet of nitrogen gas (Farley et al., 2020; Moeller et al., 2021). The targets described below as abraded targets were abraded and cleaned as described prior to scanning. Any targets described below as natural targets were neither abraded nor cleaned with the gDRT prior to scanning.

Data Analysis Procedures

We examined each individual Raman spectrum in each scan. We considered any band with a FWHM of 30 cm-1 (~3 pixels) or more a potential Raman signal. We assigned each single spectrum containing observable Raman signals to its respective mineral class via comparison to standard spectra obtained through laboratory measurements with the SHERLOC Brassboard instrument, an analogue DUV Raman and fluorescence instrument housed at the NASA Jet Propulsion Laboratory (described in detail by Razzell-Hollis et al., 2021a,b) and ACRONM (Analogue Complementary Raman for Operations oN Mars). All peak centers were determined with a Gaussian fit function, through the open-source peak fitting software Fityk (version 1.3.1; Wojdyr, 2010).

We display the SHERLOC Raman data through Raman spectral assignments overlain on each scan's associated ACI image. These spectral assignment maps are accompanied by colorized ACI images overlaid with white rings that indicate the location of each point in the scan. The spectral positioning calculations were validated from images of ACI calibration measurements where dust mobilization could be observed. Spectral map/ACI overlays are accurate to within ~44 µm near the center of maps, and within 115 µm at the 7x7 mm map corners in the HDR overlays. The points at the start of each scan (scans start at the upper left corner) have less location uncertainty than points at the end of the map scan because of robotic arm drift, which can add up to ~30 µm of uncertainty. Each laser shot hits the scanned surface as an annulus ~100 µm in diameter. The white rings overlying the colorized ACI images are ~200 µm in diameter so that the location being analyzed is visible.

Spectra Signal-to-Noise Analysis

In order to quantitatively assign confidence to SHERLOC mineral detections, we developed a statistical procedure involving comparing apparent signal intensities to a calculated median root-mean-squared-deviation (RMSD) of the noise for each scan. We first calculated the noise RMSD in the 2500–3000 cm-1 region of Raman spectra for every individual spectrum in each scan. This "silent" region was selected for its lack of signal in any spectrum, excluding cosmic ray artifacts. Then we determined the median of the noise RMSD values for each scan. We used the median to avoid contributions from any RMSD values that were inflated by cosmic rays, background fluorescence, and other spectral effects. The RMSD noise values differed between Raman images but generally occur in the 20-50 count range.

We designated single spectra Raman bands with intensities ≥3X the noise RMSD as statistically significant signals. This designation criterion is based on the International Union of Pure and Applied Chemistry's limit of detection for the probability of a data point being statistically above a normally distributed noise background (McNaught & Wilkinson, 1997). The peak position error for SHERLOC Raman bands with intensities ≥3X the noise RMSD is ≤±~4.0 cm-1. In most instances, we used mean spectra to assign detections to mineral classes. By doing so, we obtained spectra with peak intensities ≥10X the noise RMSD, which have a peak position error of <±1 cm-1.

In the context of this poster, signals with ≥3X the noise RMSD are qualitatively observed with high confidence while those <3X are observed with less confidence. For these reasons, in the ACI-Raman maps in the poster, we differentiate between Raman signals ≥3X and <3X the RMSD noise as a first-order indicator of the assignment confidence. To make this distinction, we label assignments made based on Raman signals ≥3X the noise with capital letters and those made based on signals <3X the noise with lowercase letters.

MÁAZ

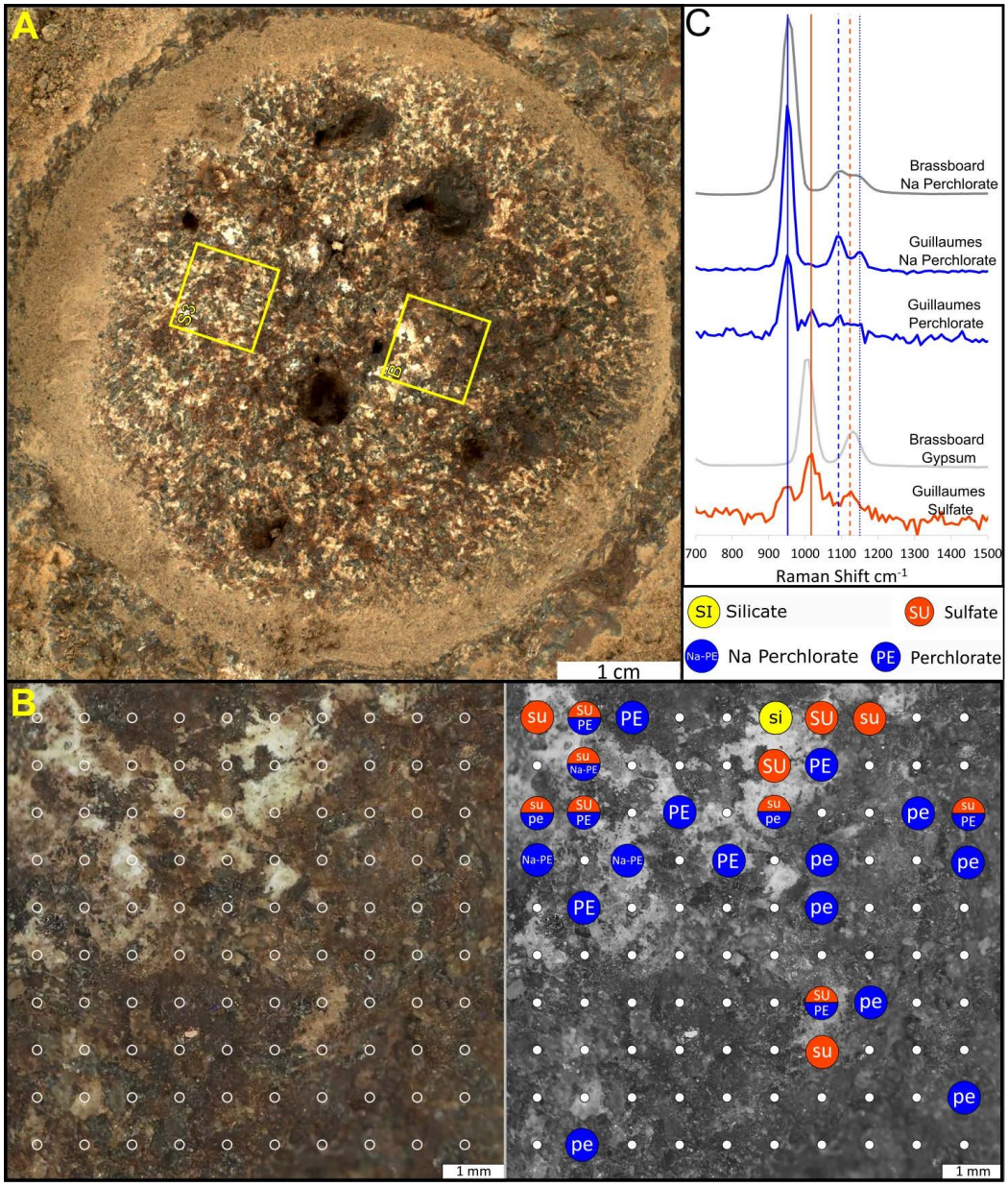

Figure 5. SHERLOC Raman mineral identifications from scan 0162_Guillaumes HDR_250_1. A) The abrasion patch imaged by WATSON (image ID SI1_0160_0681181210_679FDR_N0060000SRLC00003_000095J01). Yellow boxes indicate the location of the scans performed. The left box corresponds to HDR scans performed on sol 161 (Fig. S3). The right box corresponds to HDR scans performed on sol 162. B) colorized (left) and grayscale (right) ACI images (image ID SC3_0162_0681352993_195FDR_N0060000SRLC11420_0000LMJ01) of the region of the abrasion patch bounded by the right yellow box in panel A. The white circles in panel B indicate the locations of SHERLOC analysis spots. Mineral identifications from scan 0162_Guillaumes HDR_250_1 are indicated in the right panel. C) Representative Raman spectra of minerals detected with high confidence from the abrasion patch and spectra of mineral standards collected on the SHERLOC Brassboard instrument at JPL. Vertical lines indicate peak centers. Spectra are offset along the y-axis for clarity.

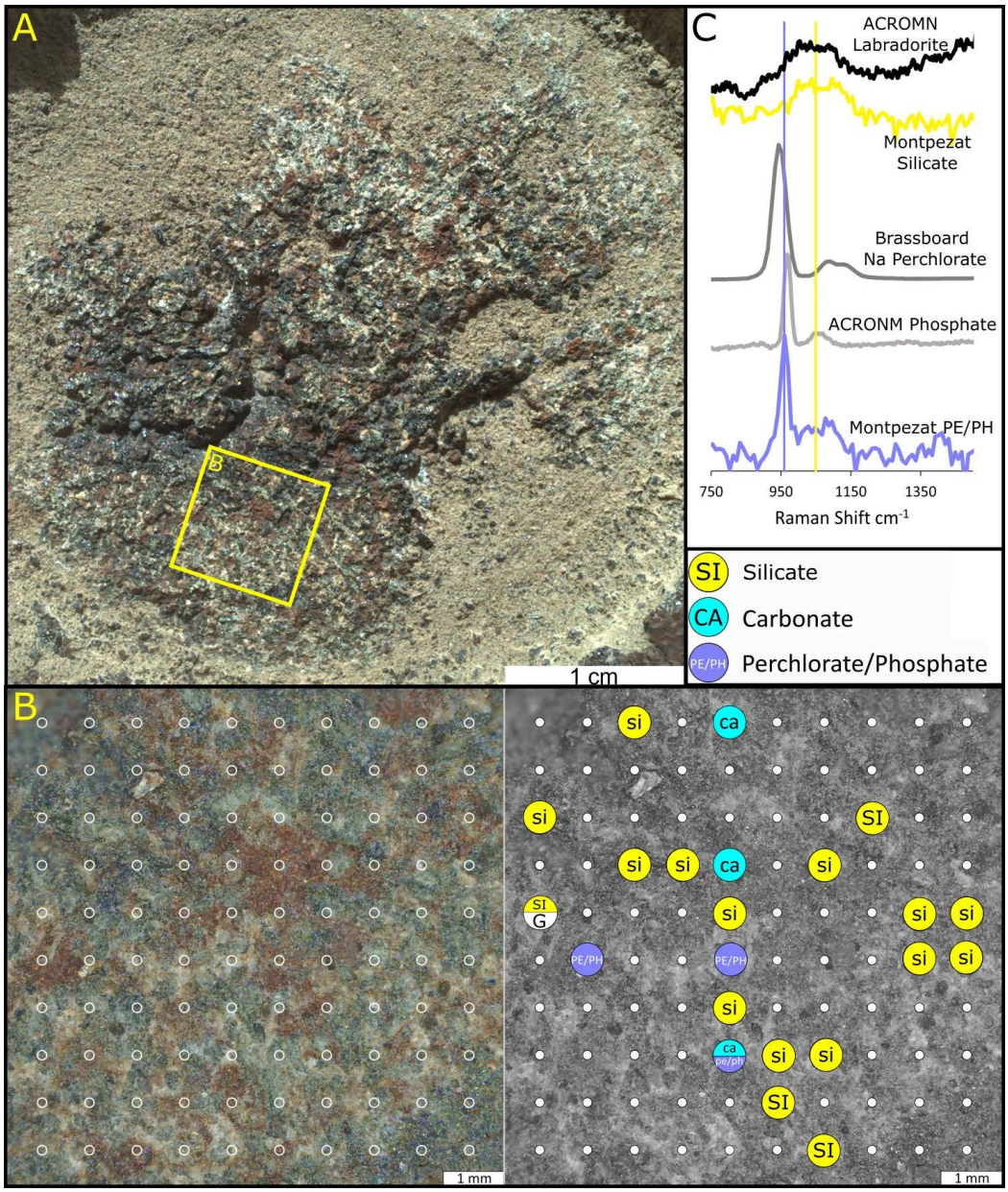

Figure 6. SHERLOC Raman mineral identifications from the 0349_Montpezat HDR_500_1 scan of target Montpezat. A) The abrasion patch imaged by WATSON (image ID SIF_0346_0697661461_972FDR_N0092982SRLC01034_0000LMJ01). The yellow box indicates the location of the scan. B) Colorized (left) and grayscale (right) ACI images (image ID SC3_0349_0697954126_179FDR_N0092982SRLC10600_0000LMJ01) of the region of the abrasion patch bounded by the yellow box in panel A. The white circles in panel B indicate the locations of SHERLOC analysis spots. Mineral identifications are indicated in the right panel. C) Representative Raman spectra from the abrasion patch of minerals detected with high confidence, and mineral standard spectra collected on the SHERLOC Brassboard instrument at JPL and the ACRONM instrument at JSC. Spectra are offset along the y-axis for clarity.

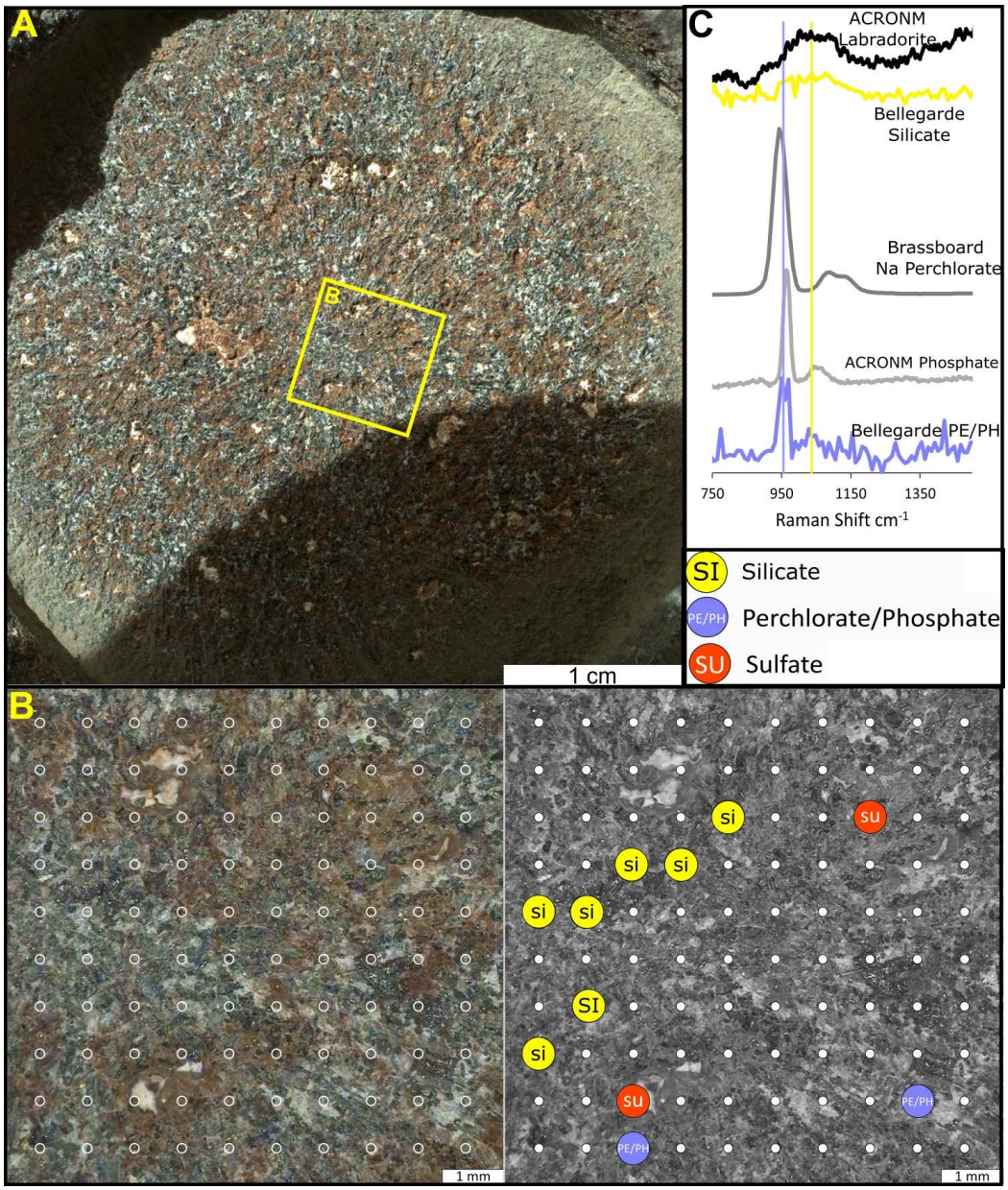

Figure 7. SHERLOC Raman mineral identifications from scan 0186_Bellegarde HDR_250_2 of the target Bellegarde. A) The abrasion patch imaged by WATSON (image ID SIF_0185_0683368184_652FDR_N0070000SRLC00720_0000LMJ01). The yellow box indicates the location of the HDR. B) Colorized (left) and grayscale (right) ACI images (image ID SC3_0186_0683479674_054FDR_N0070000SRLC11420_0000LMJ02) of the region of the abrasion patch bounded by the yellow box in panel A. The white circles in panel B indicate the locations of SHERLOC analysis spots. Mineral identifications are indicated in the right panel. C) Representative Raman spectra from the abrasion patch of minerals detected with high confidence, and mineral standard spectra collected on the SHERLOC Brassboard instrument at JPL and the ACRONM instrument at JSC) Vertical lines indicate peak centers. Spectra are offset along the y-axis for clarity.

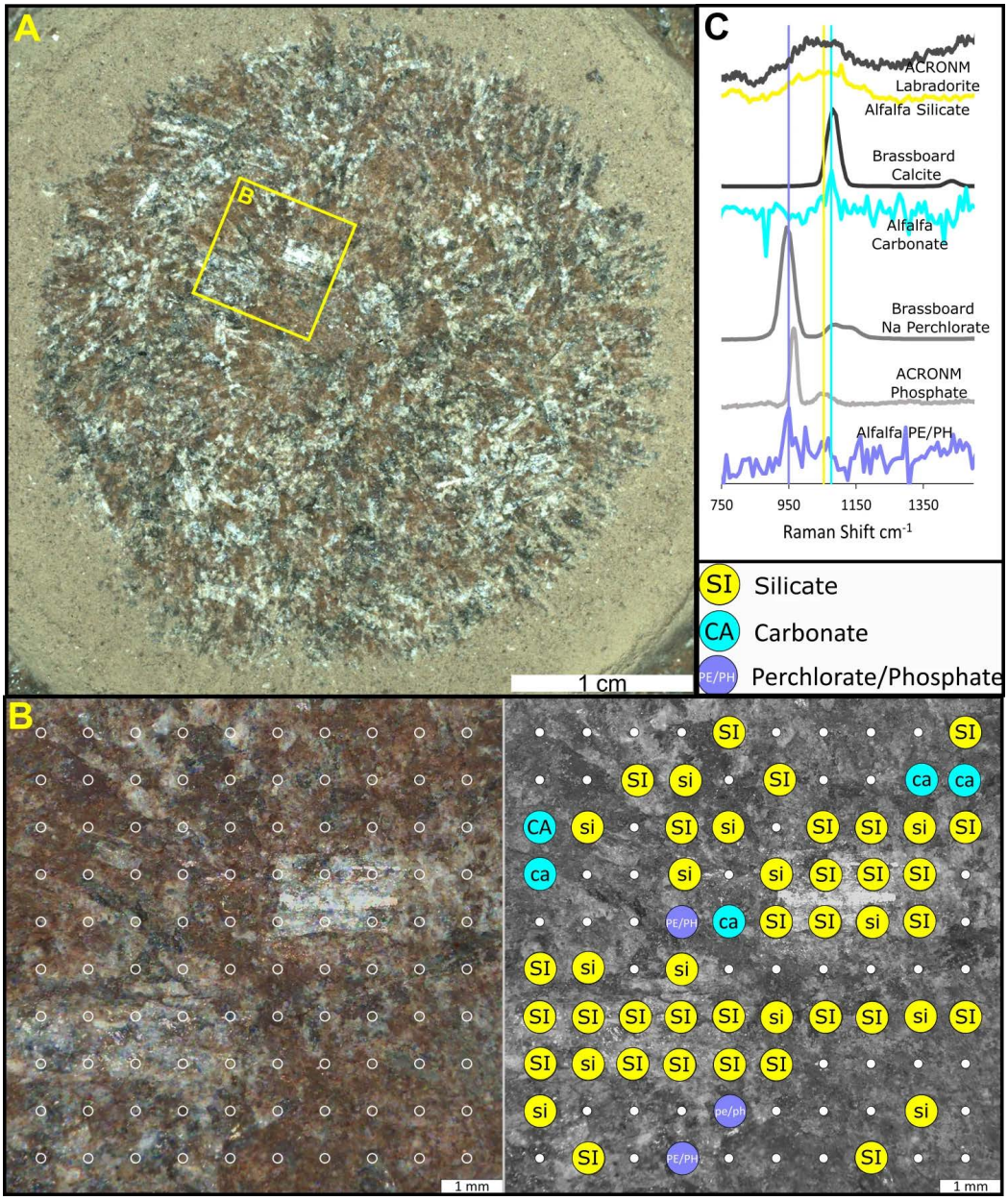

Figure 8. SHERLOC Raman mineral identifications from scan 0370_Alfalfa HDR_500_1 of target Alfalfa. A) The abrasion patch imaged by WATSON (image ID SIF_0367_0699544277_375FDR_N0110108SRLC08029_0000LMJ01). The yellow box indicates the location of the Alfalfa HDR scan. B) Colorized (left) and grayscale (right) ACI images (image ID SC3_0370_0699816293_742FDR_N0110108SRLC10600_0000LMJ01) of the region of the abrasion patch bounded by the yellow box in panel A. The white circles in panel B indicate the locations of SHERLOC analysis spots. Mineral identifications are indicated in the right panel. C) Representative Raman spectra from the abrasion patch of minerals, and mineral standard spectra collected on the SHERLOC Brassboard instrument at JPL and the ACRONM instrument at JSC. Vertical lines indicate peak centers. Spectra are offset along the y-axis for clarity.

AUTHOR INFORMATION

Andrea Corpolongo[1], Ryan S. Jakubek[2] (remaining contributors in alphabetical order) William Abbey[3], Sanford A. Asher[4], Desirée Baker[1], Luther W. Beegle[5], Eve L. Berger[6], Rohit Bhartia[7], Adrian J. Brown[3], Aaron S. Burton[8], Sergei V. Bykov[4], Emily Cardarelli[3], Edward A. Cloutis[9], Pamela Conrad[10], Andrew D. Czaja[1], Lauren DeFlores[3], David Flannery[11], Teresa Fornaro[12], Marc Fries[8], Nikole C. Haney[2], Keyron Hickman-Lewis[13,14], Linda Kah[15], Carina Lee[16], Francis M. McCubbin[8], Michelle Minitti[17], Richard V. Morris[8], Joseph Razzell Hollis[3], Ryan Roppel[4], Eva L. Scheller[18], Sunanda Sharma[3], Svetlana Shkolyar [19,20,21], Sandra Siljeström[22], Kim Steadman[3], Andrew Steele[10], Kyle Uckert[3], Brittan V. Wogsland[15], Anastasia Yanchilina[23]

1 Department of Geology, University of Cincinnati, Cincinnati, OH, USA

2 Jacobs, NASA Johnson Space Center, Houston, TX 77058, USA

3 Jet Propulsion Laboratory, California Institution of Technology, Pasadena, CA, USA

4 Department of Chemistry, University of Pittsburgh, Pittsburgh, PA, USA

5 Formerly at Jet Propulsion Laboratory, California Institution of Technology, Pasadena, CA, USA

6 Texas State University - Jacobs JETS - NASA Johnson Space Center

7 Photon Systems Incorporated, Covina, CA, USA

8 NASA Johnson Space Center, Houston, TX 77058, USA

9 Department of Geography, University of Winnipeg, Winnipeg, Manitoba, Canada

10 Carnegie Institute of Washington, Washington, DC, USA

11 Queensland University of Technology, Brisbane, Queensland, Australia

12 INAF-Astrophysical Observatory of Arcetri, Florence, Italy

13 The Natural History Museum, London, UK

14 Dipartimento BiGeA, Università di Bologna, Bologna, Italy

15 Department of Earth and Planetary Sciences, University of Tennessee, Knoxville, TN, USA

16 Lunar & Planetary Institute, Universities Space Research Association, Houston, TX, USA

17 Framework, Silver Spring, MD, USA

18 California Institute of Technology, Pasadena, CA, USA

19 USRA, Columbia, MD, USA

20 NASA Goddard Space Flight Center, Greenbelt, MD, USA

21 Blue Marble Space Institute of Science, Seattle, WA, USA

22 RISE Research Institutes of Sweden, Stockholm, Sweden

23 Impossible Sensing Incorporated, St. Louis, MO, USA

REFERENCES

This poster includes figures and modified text from a manuscript of the same name and the same authors that is currently in-review at *JGR Planets*

Beegle, L. W., Bhartia, R., Deen, Robert G., Padgett, D., Algermissen, S., Dunn, A. E., Toole, N. T., Crombie, M. K., Arena, N. W., Oij, S. L., Abarca, H. E., Slavney, S. (2021). Mars 2020 SHERLOC Bundle. NASA Planetary Data System. https://doi.org/10.17189/1522643

Bhartia, R., Beegle, L. W., DeFlores, L., Abbey, W., Razzell Hollis, J., Uckert, K., et al. (2021). Perseverance's Scanning Habitable Environments with Raman and Luminescence for Organics and Chemicals (SHERLOC) Investigation. Space Science Reviews, 217, 58. https://doi.org/10.1007/s11214-021-00812-z

Brown, A. J., Wiens, R. C., Maurice, S., Uckert, K., Tice, M., Flannery., D., et al. (2022). A Komatitite succession as an analog for the olivine bearing rocks at Jezero (abstract). 53rd Lunar and Planetary Science Conference.

Carrier, B. L., Abbey, W. J., Beegle, L. W., Bhartia, R., & Liu, Y. (2019). Attenuation of Ultraviolet Radiation in Rocks and Minerals: Implications for Mars Science. Journal of Geophysical Research: Planets, 124(10), 2599–2612. https://doi.org/10.1029/2018JE005758

Cesur, R. M., Ansari, I. M., Chen, F., Clark, B. C., & Schneegurt, M. A. (2022). Bacterial Growth in Brines Formed by the Deliquescence of Salts Relevant to Cold Arid Worlds. Astrobiology, 22(1), 104–115. https://doi.org/10.1089/ast.2020.2336

Edgett, K. S., Yingst, R. A., Ravine, M. A., Caplinger, M. A., Maki, J. N., Ghaemi, F. T., Schaffner, J. A., Bell, J. F., Edwards, L. J., Herkenhoff, K. E., Heydari, E., Kah, L. C., Lemmon, M. T., Minitti, M. E., Olson, T. S., Parker, T. J., Rowland, S. K., Schieber, J., Sullivan, R. J., … Goetz, W. (2012). Curiosity's Mars Hand Lens Imager (MAHLI) Investigation. Space Science Reviews, 170(1–4), 259–317. https://doi.org/10.1007/s11214-012-9910-4

Farley, K. A., Williford, K. H., Stack, K. M., Bhartia, R., Chen, A., de la Torre, M., Hand, K., Goreva, Y., Herd, C. D. K., Hueso, R., Liu, Y., Maki, J. N., Martinez, G., Moeller, R. C., Nelessen, A., Newman, C. E., Nunes, D., Ponce, A., Spanovich, N., … Wiens, R. C. (2020). Mars 2020 Mission Overview. Space Science Reviews, 216(8), 142. https://doi.org/10.1007/s11214-020-00762-y

Farley, K. A., Stack, K., M., Horgan, B. H. N., Tarnas, J., Sun, V. Z., Shuster, D. L., et al. (2022). Aqueously altered igneous rocks on the floor of Jezero crater, Mars. Science, https://doi.org/10.1126/science.abo2196

Fernández-Remolar, D. C., Chong-Díaz, G., Ruíz-Bermejo, M., Harir, M., Schmitt-Kopplin, P., Tziotis, D., Gómez-Ortíz, D., García-Villadangos, M., Martín-Redondo, M. P., Gómez, F., Rodríguez-Manfredi, J. A., Moreno-Paz, M., De Diego-Castilla, G., Echeverría, A., Urtuvia, V. N., Blanco, Y., Rivas, L., Izawa, M. R. M., Banerjee, N. R., … Parro, V. (2013). Molecular preservation in halite- and perchlorate-rich hypersaline subsurface deposits in the Salar Grande basin (Atacama Desert, Chile): Implications for the search for molecular biomarkers on Mars. Journal of Geophysical Research: Biogeosciences, 118(2), 922–939. https://doi.org/10.1002/jgrg.20059

Fones, E. M., Colman, D. R., Kraus, E. A., Nothaft, D. B., Poudel, S., Rempfert, K. R., Spear, J. R., Templeton, A. S., & Boyd, E. S. (2019). Physiological adaptations to serpentinization in the Samail Ophiolite, Oman. The ISME Journal, 13(7), 1750–1762. https://doi.org/10.1038/s41396-019-0391-2

Fox-Powell, M. G., & Cockell, C. S. (2018). Building a Geochemical View of Microbial Salt Tolerance: Halophilic Adaptation of Marinococcus in a Natural Magnesium Sulfate Brine. Frontiers in Microbiology, 9, 739. https://doi.org/10.3389/fmicb.2018.00739

Garczynski, B. J., Bell, J. F., Horgan, B. H. N., Johnson, J. R., Rice M. S., Vaughan, J. I., et al. (2022). Perseverance and the purple coating: A MASTCAM-Z multispectral story (abstract). 53rd Lunar and Planetary Science Conference.

Heinz, J., Krahn, T., & Schulze-Makuch, D. (2020). A New Record for Microbial Perchlorate Tolerance: Fungal Growth in NaClO4 Brines and its Implications for Putative Life on Mars. Life, 10(5), 53. https://doi.org/10.3390/life10050053

Heinz, J., Waajen, A. C., Airo, A., Alibrandi, A., Schirmack, J., & Schulze-Makuch, D. (2019). Bacterial Growth in Chloride and Perchlorate Brines: Halotolerances and Salt Stress Responses of Planococcus halocryophilus. Astrobiology, 19(11), 1377–1387. https://doi.org/10.1089/ast.2019.2069

Horgan B. H. N., Rice, M. S., Garczynski, B. J., Johnson J. R., Stack, K. M., Vaughan, J. I., et al. (2022). Mineralogy, morphology, and geochronological significance of the Máaz formation and the Jezero Crater Floor (abstract). 53rd Lunar and Planetary Science Conference.

Litasov, K. D., & Podgornykh, N. M. (2017). Raman spectroscopy of various phosphate minerals and occurrence of tuite in the Elga IIE iron meteorite. Journal of Raman Spectroscopy, 48(11).

Liu, Y., Tice, M. M., Schmidt, M. E., Treiman, A. H., Kizovski, T. V., Hurowitz, J. A., et al. (2022). An olivine cumulate outcrop on the floor of Jezero crater, Mars. Science, https://doi.org/10.1126/science.abo2756

McNaught, A. D., Wilkinson, A. (1997). Compendium of chemical terminology. Blackwell Science.

Meslin, P.-Y., Forni, O., Beck, P., Cousin, A., Beyssac, O., Lopez-Reyes, G., et al.. (2022). Evidence for perchlorate and sulfate salts in Jezero Crater, Mars, from SuperCam observations (abstract). 53rd Lunar and Planetary Science Conference.

Moeller, R. C., Jandura, L., Rosette, K., Robinson, M., Samuels, J., Silverman, M., et al. (2021). The Sampling and Caching Subsystem (SCS) for the Scientific Exploration of Jezero Crater by the Mars 2020 Perseverance Rover. Space Science Reviews, 217(1), 5. https://doi.org/10.1007/s11214-020-00783-7

Morris, R. V., Haney, N. C., Jakubek, R. S., Fries, M. D., Clark, J. V., Lee, L., and Mertzman, S. A. (2022). Relative detectability of iron-bearing phases for the Mars 2020 SHERLOC deep UV Raman instrument: 1. Focusing on carbonates (abstract). 53rd Lunar and Planetary Science Conference.

Núñez, J. I., Johnson J. R., Horgan B. H. N., Rice M. S., Vaughan A., Tate, C., et al. (2022).Stratigraphy and mineralogy of the deposits within Séítah region on the floor of Jezero Crater, Mars as seen with Mastcam-Z (abstract). 53rd Lunar and Planetary Science Conference.

Razzell Hollis, J., Abbey, W., Beegle, L. W., Bhartia, R., Ehlmann, B. L., Miura, J., Monacelli, B., Moore, K., Nordman, A., Scheller, E., Uckert, K., & Wu, Y.-H. (2021a). A deep-ultraviolet Raman and Fluorescence spectral library of 62 minerals for the SHERLOC instrument onboard Mars 2020. Planetary and Space Science, 209, 105356. https://doi.org/10.1016/j.pss.2021.105356

Razzell Hollis, J., Ireland, S., Abbey, W., Bhartia, R., & Beegle, L. W. (2021b). Deep-ultraviolet Raman spectra of Mars-relevant evaporite minerals under 248.6 nm excitation. Icarus, 357, 114067. https://doi.org/10.1016/j.icarus.2020.114067

Scheller, E.L., Razzell Hollis, J., Cardarelli, E. L., Steele, A., Beegle, L. W., Bhartia, R., et al. (2022). Aqueous alteration processes and implications for organic geochemistry in Jezero crater, Mars. Science.

Schmidt, M. E., Allwood A., Christian, J., Clark, B. C., Flannery, D., Hennecke, J., et al. (2022). Highly differentiated basaltic lavas examined by PIXL in Jezero Crater (abstract). 53rd Lunar and Planetary Science Conference.

Schopf, J. W., Farmer, J. D., Foster, I. S., Kudryavtsev, A. B., Gallardo, V. A., & Espinoza, C. (2012). Gypsum-Permineralized Microfossils and Their Relevance to the Search for Life on Mars. Astrobiology, 12(7), 619–633. https://doi.org/10.1089/ast.2012.0827

Shkolyar, S., & Farmer, J. D. (2018). Biosignature Preservation Potential in Playa Evaporites: Impacts of Diagenesis and Implications for Mars Exploration. Astrobiology, 18(11), 1460–1478. https://doi.org/10.1089/ast.2018.1849

Stack, K. M., et al. (2020). Photogeologic Map of the Perseverance Rover Field Site in Jezero Crater Constructed by the Mars 2020 Science Team. Space Science Reviews, 216(8), 127. https://doi.org/10.1007/s11214-020-00739-x

Sun, V. Z., Hand, K. P., Stack, K. M., Farley, K. A., Milkovich, S., Kronyak, R., et al. (2022). Exploring the Jezero Crater floor: Overview of results from the Mars 2020 Perseverance Rover's first science campaign (abstract). 53rd Lunar and Planetary Science Conference.

Twing, K. I., Brazelton, W. J., Kubo, M. D. Y., Hyer, A. J., Cardace, D., Hoehler, T. M., McCollom, T. M., & Schrenk, M. O. (2017). Serpentinization-Influenced Groundwater Harbors Extremely Low Diversity Microbial Communities Adapted to High pH. Frontiers in Microbiology, 8. https://doi.org/10.3389/fmicb.2017.00308

Uckert, K., Bhartia, R., Beegle, L. W., Monacelli, B., Asher, S. A., Burton, A. S., Bykov, S. V., Davis, K., Fries, M. D., Jakubek, R. S., Hollis, J. R., Roppel, R. D., & Wu, Y.-H. (2021). Calibration of the SHERLOC Deep Ultraviolet Fluorescence–Raman Spectrometer on the Perseverance Rover. Applied Spectroscopy, 75(7), 763–773. https://doi.org/10.1177/00037028211013368

Udry, A., Sautter, V., Cousin, A., Wiens, R. C., Forni, O., Benzerara, K., et al. (2022). A Mars 2020 Perseverance SuperCam perspective on the igneous nature of the Máaz formation at Jezero crater, Mars (abstract). 53rd Lunar and Planetary Science Conference.

Wiens, R. C., Udry, A., Mangold, N., Beyssac, O., Quantin, C., Sautter, V., et al. (2022). Composition and density stratification observed by SuperCam in the first 300 sols in Jezero Crater (abstract). 53rd Lunar and Planetary Science Conference.

Wojdyr, M. (2010). Fityk: A general-purpose peak fitting program. Journal of Applied Crystallography, 43(5), 1126–1128. https://doi.org/10.1107/S0021889810030499

Woycheese, K. M., Meyer-Dombard, D. R., Cardace, D., Argayosa, A. M., & Arcilla, C. A. (2015). Out of the dark: Transitional subsurface-to-surface microbial diversity in a terrestrial serpentinizing seep (Manleluag, Pangasinan, the Philippines). Frontiers in Microbiology, 6. https://doi.org/10.3389/fmicb.2015.00044

Xing, T., Zhu, W., Fusseis, F., & Lisabeth, H. (2018). Generating porosity during olivine carbonation via dissolution channels and expansion cracks. Solid Earth, 9(4), 879–896. https://doi.org/10.5194/se-9-879-2018